processes

MDPI

Article

Fabrication of NiO-CuO/RGO Composite for Lithium Storage Property

Yuanxiang Fu [1,2,*], Yuxin Chen [1,3], Fan Wang [1] and Guoyong Zhou [3,*]

[1] School of Chemical Engineering & Key Laboratory of Energy Chemistry in Guizhou Universities, Guizhou Institute of Technology, Guiyang 550003, China; cyx@gzmu.edu.cn (Y.C.); 826436676@git.edu.cn (F.W.)
[2] Guangdong Engineering Technology Research Centre for Advanced Thermal Control Material and System Integration (ATCMSI), Guangzhou 510275, China
[3] School of Chemical Engineering, Guizhou Minzu University, Guiyang 550025, China
* Correspondence: fuyx8@git.edu.cn (Y.F.); gyzhou@gzmu.edu.cn (G.Z.)

Abstract: The lithium storage performance of binary transition metal oxide/graphene composites as anode materials has been attracting more interest from researchers, based on the fact that binary transition metal oxides and graphene are expected to create a synergistic effect and exhibit improved lithium storage characteristics. In this work, a NiO-CuO/reduced graphene oxide composite (NiO-CuO/RGO) was prepared by an ultrasonic agitation process. When the NiO-CuO/RGO is applied to the anode material for lithium-ion batteries (LIBs), the batteries display high discharge capacities (at 730 mA h/g after 100 cycles at 100 mA/g), high-rate performance (311 mA h/g with 5000 mA/g), and excellent stable cyclability (375 mA h/g within 2000 mA/g after 400 cycles). Such results indicate that the combination of NiO-CuO and RGO leads to enhanced lithium storage performance, for the RGO sheets inhibit the large volume change of binary NiO-CuO and enhance the fast transport of both lithium ions and electrons during the repeated lithium cycling processes.

Keywords: NiO-CuO/RGO; lithium storage property; synergistic effect

Citation: Fu, Y.; Chen, Y.; Wang, F.; Zhou, G. Fabrication of NiO-CuO/RGO Composite for Lithium Storage Property. *Processes* **2024**, *12*, 1422. https://doi.org/10.3390/pr12071422

Academic Editor: Qunjie Xu

Received: 15 May 2024
Revised: 22 June 2024
Accepted: 27 June 2024
Published: 8 July 2024

1. Introduction

As power sources, lithium-ion batteries (LIBs) have been extensively used in portable electronics, electric vehicles, and storage systems for renewable energy [1,2]. However, the increasing development of high-performance electric vehicles requires next-generation LIBs with high energy density and long-term cycling performance characteristics [3–5]. However, the commercial graphite anode has been hindered in the above-mentioned application requirements owing to its relatively low theoretical specific capacity (372 mA h/g). Therefore, it is necessary to explore novel anode materials to meet the application requirements for next-generation LIB development.

In view of the high theoretical capacity of NiO, and the synergetic effect of NiO and other oxide components, binary nickel-based oxides (NiO/ZnO [6,7], NiO/Fe_2O_3 [8,9], NiO/Co_3O_4 [10], NiO/MnO_2 [11], and NiO/CuO [12]) have inspired great interest from researchers as anode candidates for LIBs. Meanwhile, the ionic/electronic transport at the solid–solid heterojunction lead to a mild stepwise lithiation and de-lithiation process during the charge/discharge processes for the synergistic effects of NiO and other oxides [13,14], and the expression can be beneficial to enhance the lithium storage property of a cell. Nonetheless, like pure NiO, the application of binary nickel-based oxides for LIBs are hindered by their poor electronic conductivity and large volume change in the repeated lithium cycling processes due to the conversion reaction, which results in a short service life and fast lithium storage capacity decay. To overcome such shortcomings, one effective approach is to decorate binary nickel-based oxides with conductive carbon materials. As a typical two-dimensional carbon material, graphene has mechanical and electrical

performances, and it can improve the ionic/electronic transport capacity of binary nickel-based oxides with its flexible layered structure, strong mechanical properties [15–17], and high-conductivity properties. In addition, graphene is able to suppress the volume changes of binary nickel-based oxides during repeated lithium cycling processes [18–20]. To our knowledge, there have been only a few reports of the use of a NiO-CuO/graphene anode material for LIBs in the existing literature [21]. Therefore, we combine NiO-CuO with reduced graphene oxide sheets to develop a high-performance anode material for LIBs.

In this study, a NiO-CuO and reduced graphene oxide (NiO-CuO/RGO) composite was designed and produced by annealing a nickel hydroxide–copper hydroxide composite with GO sheets (Ni $(OH)_2$-Cu $(OH)_2$/GO), which was synthesized via an ultrasonic agitation method. It is confirmed that NiO-CuO/RGO applied as an anode material for LIBs can exhibit excellent lithium storage performance, and has a reversible capacity of 730 mA h/g at 100 mA/g after 100 cycles, and a favorable rate capability of 438 mA h/g and 311 mA h/g at 2000 and 5000 mA/g, respectively. Additionally, a high reversible capacity of 375 mA h/g was obtained at 2000 mA/g after 400 cycles, which could be benefited by the RGO sheets restraining the volume change of NiO-CuO and facilitating the fast transport of Li^+ and electrons during the discharge/charge processes.

2. Materials and Methods

2.1. Materials Synthesis

Graphene oxide (GO) was prepared according to a modified Hummers method with some adjustments [22,23]. The NiO-CuO/RGO composite was fabricated using an ultrasonic stirring method after calcination treatment. A solution of 120 mg GO powder, 60 mL deionized water, and 120 g polyvinylpyrrolidone (PVP) underwent ultrasonication for 45 min with mechanical stirring. Then, 5mmol Ni $(NO_3)_2 \cdot 6H_2O$ and 5 mmol Cu $(NO_3)_2 \cdot 6H_2O$ were dissolved in the dispersed GO solution with magnetic stirring. Subsequently, 12 mL 25% aqueous ammonia was dropwise added into the above solution with vigorous stirring and ultrasonic treatment for 5 h. The Ni $(OH)_2$-Cu $(OH)_2$/GO precursor was obtained, and then the precursor was washed several times with distilled water. Finally, the NiO-CuO/RGO composite was obtained after the calcination of the dried Ni $(OH)_2$-Cu $(OH)_2$/GO precursor at 350 °C for 4 h with a nitrogen atmosphere and a ramping rate of 5 °C/min. For comparison, the NiO-CuO was prepared using the same method without the GO.

2.2. Characterization

The crystal data of the as-prepared samples were characterized by X-ray diffraction (XRD, Rigaku D-MAX 2200 VPC) with Cu Ka radiation. Thermogravimetric analysis (TG) of the NiO-CuO and NiO-CuO/RGO was conducted using a thermal analysis apparatus (TG, 209 F3 Tarsus), and N_2 adsorption/desorption isotherms were obtained using a Micromeritics ASAP 2460 at a temperature of 77 K. The morphologies of the samples were measured using a transmission electron microscope (TEM, JEOL-2010 HR) and a scanning electron microscope (SEM, FEI-Q400F) with an energy dispersive spectrometer (EDS). An X-ray photo-eletron spectroscopy (XPS) measurement was conducted using an ESCALAB 250 spectrometer with an Al Ka X-ray source.

2.3. Electrochemical Measurements

The electrochemical performances of the as-prepared samples were measured using coin-type half cells (CR-2032-type). The working electrodes were prepared by mixing 75 wt% active material, 15 wt% conductive additive of carbon black (Super P), and 10 wt% polyvinylidene fluoride (PVDF). And an appropriate amount of N-methyl-2-pyrrolidone solvent was used as the PVDF binder. The homogeneous paste was spread onto a copper foil and dried at 120 °C for 12 h in vacuum oven. The cells were assembled in an argon-filled glove box using the as-prepared working electrodes, lithium foil as the counter electrode, Celgard 2400 polypropylene micro-porous film as the separator, and 1 M $LiPF_6$

in a mixture of ethylene carbonate (EC) and dimethyl carbonate (DME) 1:1 (*vol*/*vol*) as the electrolyte. Galvanostatic charge/discharge tests were performed on a LAND battery test system (LAND, CT2001A) in the range of 0.01–3.0 V (vs. Li/Li^+). Cyclic voltammetry (CV) was evaluated on an electrochemical workstation (Chenhua, CHI660E) with a scan rate of 0.1 mV/s between 0.01 and 3 V (vs. Li/Li^+). The electrochemical impedance spectrum (EIS, 1 MHz to 0.1 Hz) measurements were verified using an electrochemical workstation (Chenhua, CHI660E).

3. Results

The Ni $(OH)_2$-Cu $(OH)_2$/GO precursor was prepared using cupric nitrate, nickel nitrate, and a GO solution via an ultrasonic agitation method. The SEM images show the precursor with a flake-like structure (Figure S1), and the XRD result indicates that a diffraction peak of $2\theta \approx 10^\circ$ on the curve is well-assigned to GO [23]. In addition, the weak diffraction peaks of Cu $(OH)_2$ [24] and Ni $(OH)_2$ [25] are also observed on the curve of the composite (Figure S2). Figure 1a shows the XRD patterns of the NiO-CuO and NiO-CuO/RGO samples. The NiO-CuO exhibited all of the characteristic peaks of NiO ($2\theta \approx 37.1^\circ$, 43.2°, 62.7°, 75°, and 78.6°, JCPDS card No. 65-2901) [26,27], and sharp characteristic peaks of CuO ($2\theta \approx 32.4^\circ$, 35.5°, 38.7°, 38.9°, 48.6°, 53.4°, 58.3°, 61.4°, 65.7°, 66.1°, and 68°, JCPDS card No. 80-1917) [28,29]. The standard peaks of pure NiO and CuO, and a weak diffraction peak at 26° which can be ascribed to the RGO sheets, were observed on an XRD curve of the NiO-CuO/RGO composite sample. The NiO-CuO specimen with smaller flake-like structures, as shown in the SEM image (Figure 1b), and some small particles were also observed in the amplified image (Figure 1c). Figure 1d shows that the NiO-CuO/RGO composite with flake-like morphology around a length of 1~3 μm, and many NiO-CuO flakes, were anchored on the surface of the RGO sheets (Figure 1e). Thermogravimetric analysis (TGA) curves of NiO-CuO and the NiO-CuO/RGO composite in air between room temperature and 850 °C are provided in Figure 1f. The mass loss of approximately 7.62% of NiO-CuO can be attributed to the removal of adsorbent substances and adsorbed water before 200 °C, and the mass loss of 4.96% from 200 to 850 °C is due to the decomposition of NiO. The mass loss of around 6.73% of the NiO-CuO/RGO composite can be attributed to the removal of adsorbent substances and adsorbed water due to the existence of the RGO sheets under 200 °C, and the total mass loss of the sample was around 33.56% between 200 and 850 °C, which can be ascribed to the decomposition of the NiO and RGO sheets [20]. Additionally, compared with the TGA result of the NiO-CuO, we could calculate that the RGO content in the NiO-CuO/RGO was around 28.6%.

The energy dispersive spectrometer (EDS) spectrum of the NiO-CuO/RGO composite is shown in Figure 2a. There are certain amounts of C, O, Ni, and Cu elements in the sample, and all the elements are uniformly distributed in the as-prepared sample (bottom of Figure 2a); the result shows that the NiO-CuO/RGO composite has a uniform structure. That the NiO-CuO is well-anchored on the surface of the RGO sheets can be further confirmed by the TEM image (Figure 2b), and the amplified image reveals the NiO-CuO has a flake-like shape with a length of 20~100 nm (Figure 2c). The high-resolution transmission electron microscopy (HRTEM) image displays NiO and CuO on the RGO sheets, and the lattice fringe interplanar distance of NiO is 0.21 nm (200). Additionally, 0.25 nm (002) of CuO [30] was also detected, as shown in Figure 2d. The selected area electron diffraction (SAED) pattern (top left-hand corner of Figure 2d) shows well-resolved diffraction rings, which can be indexed to the (002) and (111) planes of CuO [31], and the (200) and (220) planes of NiO [32], again indicating the existence of CuO and NiO on the RGO sheets.

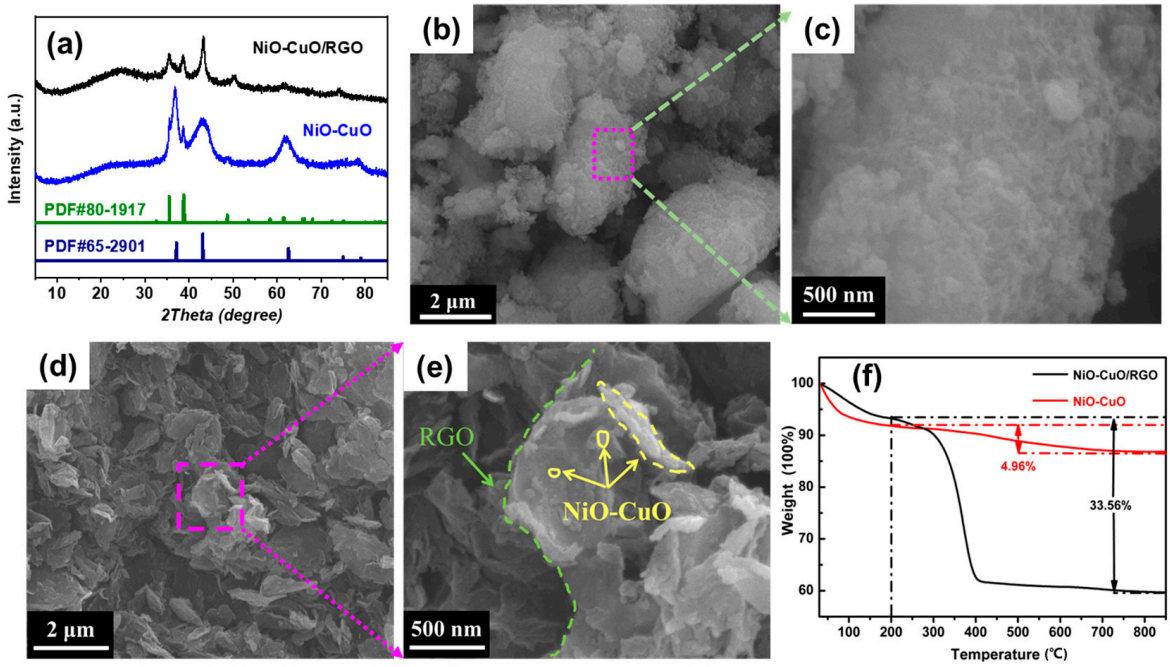

Figure 1. XRD patterns of NiO-CuO and NiO-CuO/RGO (**a**), low and magnified SEM images of NiO-CuO (**b**,**c**) and NiO-CuO/RGO (**d**,**e**), and TGA curves of pure NiO-CuO and NiO-CuO/RGO composite (**f**).

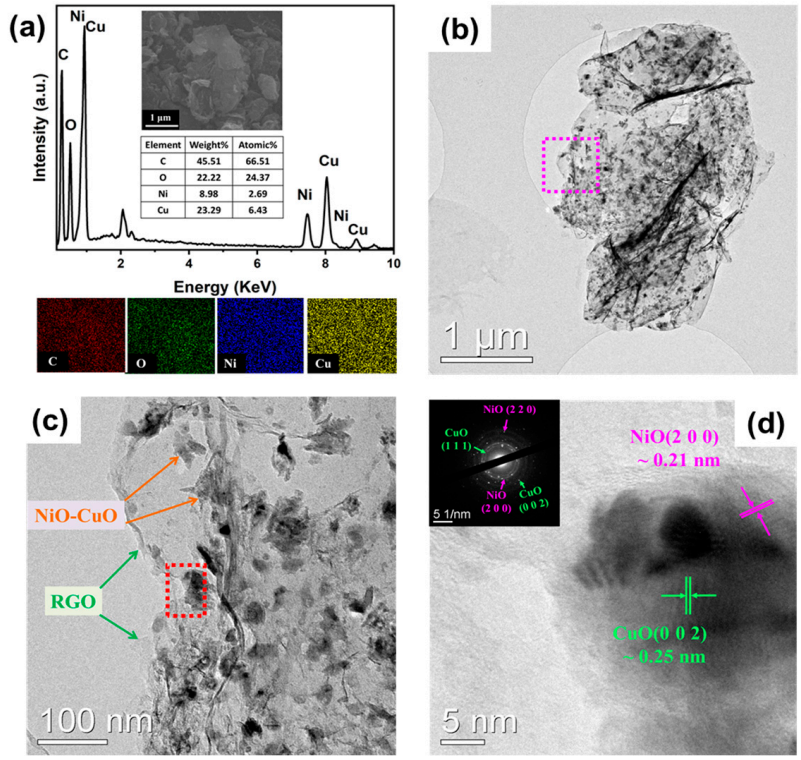

Figure 2. (**a**) EDS and the corresponding elemental mapping images, the low (**b**,**c**) and high (**d**) magnified TEM images of the NiO-CuO/RGO composite.

The chemical ingredients and oxidation states of NiO-CuO/RGO are confirmed by X-ray photoelectron spectroscopy (XPS) analysis. The full XPS spectra of C 1s, O 1s, Ni 2p, and Cu 2p can be clearly observed in Figure 3a, indicating the presence of C, O, Ni, and Cu elements in the specimen. For the high-resolution XPS spectra of C1s, three peaks located at

284.8, 285.7, and 288.6 eV are assigned to C-C, C-O, and O=C-O, respectively [33]. The O1s spectrum can be divided into three peaks at 530, 531.5, and 532.7 eV, which are ascribed to the lattice oxygen, O=C, and O-C, respectively [27]. As for the high-resolution Ni 2p spectrum, two major peaks occurred at 855.6 eV and 873.3 eV and were assigned to the Ni 2p3/2 and Ni 2p1/2 peaks, respectively. The satellite peaks of Ni^{2+} were 861.2 eV and 879.5 eV [34,35]. Finally, in the Cu 2p XPS spectra, two peaks derived from Cu 2p3/2 and Cu 2p1/2 peaks were found at 934.5 eV and 954.5 eV, respectively, implying the presence of CuO in the composite. The N_2 adsorption/desorption isotherm is used to study the porosity of the NiO-CuO/RGO composite. The Brunauer–Emmett–Teller (BET) surface area of NiO-CuO/RGO is 79.6 m^2/g, and the pore size distribution with two areas is at 0~20 and 20~140 nm in the sample. Additionally, it is noted that the BET surface area value of the NiO-CuO sample is only 5.3 m^2/g, maybe due to the absence of RGO sheets.

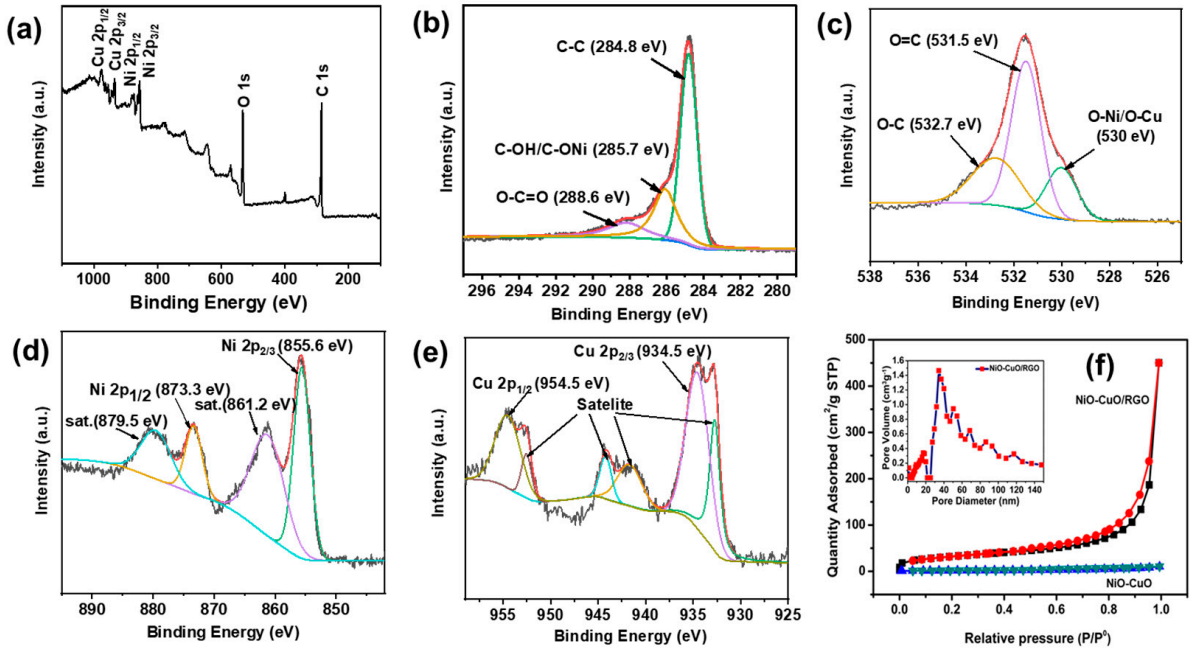

Figure 3. XPS spectra of the NiO-CuO/RGO composite: (**a**) survey, (**b**) C 1s, (**c**) O1s, (**d**) Ni 2p, (**e**) Cu 2p, and (**f**) N_2 adsorption/desorption isotherms and the corresponding pore size distribution.

To investigate the electrochemical performances of the as-prepared samples as anode materials, lithium-ion half cells of all samples were assembled in a glove box with ultra-low water oxygen content. Figure 4a shows that the initial five cyclic voltammetry (CV) curves of the NiO-CuO/RGO sample range from 0.01 V to 3 V vs. Li/Li^+ at a scan rate of 0.1 mV/s. An obvious peak exists at 1.52 V, as does a peak at 1.15 V in the first cathodic scan, which may be ascribed to the formation of the Cu_2O phase, because Cu is involved in the electrochemical reaction [36]. Another peak located at 0.54 V is attributed to the reduction of Ni^{2+} to Ni^0 and the formation of the solid electrolyte interface (SEI) layer [37]. In the reversible process, the anodic peaks at 2.19 V and 2.46 V can be ascribed to the oxidation reactions of metallic Ni [38] and Cu_2O [39,40]. Additionally, there is a peak at 1.28 V, indicating that it may relate to Li-ion deintercalation from graphitic layers [41,42]. In the subsequent cycles, the anodic peak conversion of NiO into Ni shifts to 0.89 V, and the other peaks exhibit a high degree of coincidence in the curves, which indicates that the battery has excellent cyclability and stability. Certainly, we also noticed that the location of the CV oxidation/reduction peaks of the NiO-CuO/RGO sample was slightly displaced in comparison with that of pure CuO and NiO samples, which might be caused by the

coordination between the two substances [43,44]. The charge and discharge processes of the NiO-CuO/RGO electrode can be attributed to the following reactions [12,21,45]:

$$NiO + 2Li^+ + 2e^- \leftrightarrow Ni + Li_2O \quad (1)$$

$$CuO + 2Li^+ + 2e^- \leftrightarrow Cu + Li_2O \quad (2)$$

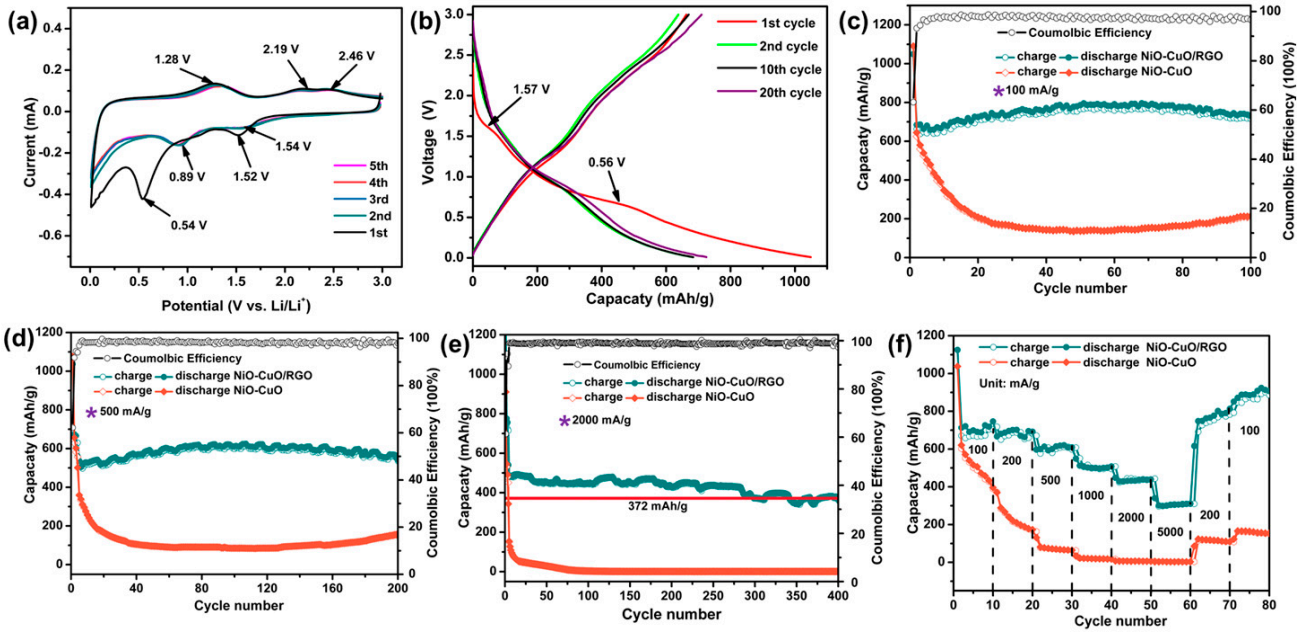

Figure 4. (**a**) CV curves of NiO-CuO/RGO, (**b**) galvanostatic charge-discharge profiles of NiO-CuO/RGO at 100 mA/g, cycling performances of NiO-CuO and NiO-CuO/RGO at 100 mA/g (**c**), 500 mA/g (**d**), and 2000 mA/g (**e**), respectively, and (**f**) rate performance of NiO-CuO and NiO-CuO/RGO.

The repeated discharge–charge voltage curves of the electrode range from 0.01 to 3 V at a current density of 100 mA/g, as shown in Figure 4b. The first discharge cycle voltage platform at 1.57 V and 0.56 V was well consistent with the first-cycle CV result. Additionally, the first discharge and charge capacities of the NiO-CuO/RGO electrode are 1049 mA h/g and 663 mA h/g, respectively, and the initial coulombic efficiency (CE) is around 63%. We considered that the initial capacity loss was due to the formation of the solid electrolyte interphase (SEI) layer and some undetermined irreversible reactions [21]. Fortunately, the CE of the NiO-CuO/RGO electrode rapidly enhanced after 10 cycles, and the CE even reached up to 96.2% after 20 cycles. The cycle performances for the NiO-CuO and NiO-CuO/RGO electrodes at 100 mA/g are provided in Figure 4c. The simple NiO-CuO electrode displays a rapid capacity loss, and only 215 mA h/g can be retained after 100 cycles. Such poor cycle stability behavior is well consistent with the result of early reported NiO-based composites due to the pulverization caused by the large volume change. Moreover, the reversible capacity of the NiO-CuO specimen is higher than that of the pure NiO sample in our previous report, which may be attributed to an asynchronous lithium reaction resulting from the weak volume variation for the binary NiO-CuO oxides with different redox potentials [20]. We notice that the capacity of the NiO-CuO/RGO electrode shows a stable cyclability, and it also maintains a high reversible capacity above 730 mA h/g after 100 cycles, which is significantly higher than that of NiO-CuO specimen. Additionally, the cycle stability is better than the NiO-CuO nanocomposites [12], the CuO-doped NiO/carbon nanotube nanocomposite [21], and the 3D graphene-encapsulated ZnO-NiO-CuO [27]. Moreover, the NiO-CuO/RGO electrode shows a result of 542 mA h/g at 500 mA/g after 200 cycles and a high coulombic efficiency (CE) of 99%. To further verify

the cycle stability of the NiO-CuO/RGO electrode, we tested the battery at 2000 mA/g for 500 cycles, and the reversible capacity could be maintained at 375 mA h/g. This value is slightly higher than the theoretical capacity of a commercial graphite anode. Figure 4e shows the rate capabilities of NiO-CuO and NiO-CuO/RGO at a current range from 100 to 5000 mA/g. The reversible capacity of the NiO-CuO/RGO electrode at the sixth cycle is 691, 670, 614, 521, 472, and 311 mA h/g when the current density is at 100, 200, 500, 1000, 2000, and 5000 mA/g, respectively. Remarkably, a high capacity of 875 mA h/g could be recovered when the current density returned to 100 mA/g, and the electrode displayed that the high reversible capacity had largely increased from the first ten cycles at 100 mA/g, which might mean the electrode had more active lithium storage sites after the action of a high current (at 5000 mA/g) [44]. By contrast, the NiO-CuO capacity quickly faded upon cycling with the increasing current densities. We noticed that when the current density was 5000 mA/g, the capacity of the NiO-CuO/RGO electrode was 311 mA h/g, which is much higher than the capacity of the NiO-CuO sample (4 mA h/g). The excellent electrochemical performance of the NiO-CuO/RGO electrode can be ascribed to the unique flake-like architecture of NiO-CuO/RGO, which better riveted the NiO-CuO flake onto the surface of the RGO sheets, and restrained the NiO-CuO flakes from peeling off from the RGO sheets during the charge/discharge process caused by volume change [27,46]. Furthermore, the RGO sheets can form a conductive network to improve the electrical conductivity of the electrode, and facilitate both the Li^+ diffusion rate and electron transport. The RGO sheets can further alleviate the stress of NiO-CuO flakes that is created during repeated lithiation/de-lithiation processes, while maintaining the structural integrity [47]. Meanwhile, the ammonia and the graphene might to form a stable chemical bond after the long-time ultrasonic treatment process, which can be effectively fixed NiO-CuO particles to the surface of rGO sheets with physical adsorption and chemical bond for the transport of ions and electrons in the electrode during charge and discharge processes. Compared with other NiO-based samples [18,19,48], the NiO-CuO/RGO electrode also displayed competitive lithium storage performances.

The EIS result provided additional evidence to support the outstanding electrochemical performance of the NiO-CuO/RGO composite. As shown in Figure 5a, the semicircle of the NiO-CuO/RGO electrode is obviously smaller than that of the NiO-CuO electrode at different frequencies. The modeled equivalent circuit of the electrode can be seen in Figure 5a. The charge transfer resistance (Rct = 52 Ω) of the NiO-CuO/RGO is 355 Ω, which is lower than that of the simple NiO-CuO electrode. It can be determined that the lower resistance of the NiO-CuO/RGO electrode can benefit from the RGO sheets, which can construct a crosslinked conductive network and capture the NiO-CuO nanosheets on the surface to improve the electronic conductivity of the electrode [20]. Therefore, excellent cycling stability and rate capability of the electrode can be obtained in different current densities. It can be observed that the NiO-CuO/RGO sheets and carbon black particles are uniformly distributed in the initial electrode in Figure 5b (as shown the red arrow area). Nevertheless, it is evident from the yellow arrow area in Figure 5c,d that the NiO-CuO/RGO swelled notably after 400 charge-discharge cycles at 2000 mA/g, indicating that the volume expansion of the NiO-CuO/RGO sheets occurred during the repeated lithium insertion/extraction processes after 400 cycles, which is caused by the fading of the lithium storage capacity of the electrode(as shown the red arrow area). Finally, the Nyquist plots of NiO-CuO/RGO electrodes before and after the cycles show that the charge transfer resistance of the 400th electrode is bigger than that of the initial electrode (Figure S3), which also supports the above-mentioned conclusions.

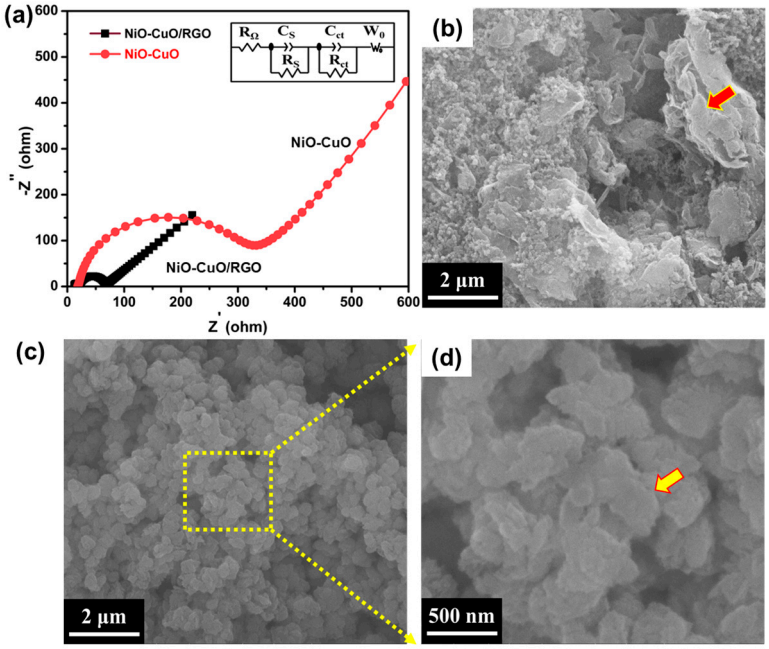

Figure 5. (**a**) the Nyquist plots for EIS of the NiO-CuO and NiO-CuO/RGO, SEM images of NiO-CuO/RGO electrode (**b**) before and (**c**,**d**) after 400 charge/discharge cycles at 2000 mA/g.

4. Conclusions

In summary, a flake-like NiO-CuO/RGO composite was fabricated via an ultrasonic agitation method after calcination treatment. When the sample was used as an anode for LIBs, a high reversible capacity of 730 mA h/g after 100 cycles at 100 mA/g was obtained, and a high reversible capacity at 375 mA h/g of the electrode can be maintained at 2000 mA/g after 400 cycles. The electrode also displayed a fascinating rate capability that was much higher than the pure NiO-CuO electrode. The excellent lithium storage performance of the NiO-CuO/RGO composite can be ascribed to the unique flake-like structure of the sample and the strong anchoring of NiO-CuO on the surface of the RGO sheets. And the RGO sheets can also suppress the volume change of the NiO-CuO and facilitate the fast transport of Li^+ and electrons of the NiO-CuO/RGO electrode during the repeated charge/discharge processes.

Supplementary Materials: The following supporting information can be downloaded at: https://www.mdpi.com/article/10.3390/pr12071422/s1, Figure S1: Low (a) and high (b) magnification SEM images of Ni $(OH)_2$-Cu $(OH)_2$/GO sample.; Figure S2: XRD pattern of Ni $(OH)_2$-Cu $(OH)_2$/GO sample. title; Figure S3 Nyquist plots of NiO-CuO/RGO electrode before and after 400 cycles at 2000 mA/g.

Author Contributions: Conception, editing, obtain research funding, Y.F.; experiment, data analysis, editing, Y.C.; experiment, data analysis, F.W.; conception, writing—review, G.Z. All authors have read and agreed to the published version of the manuscript.

Funding: The authors gratefully acknowledge financial support for this research by the high-level talent scientific research startup project of the Guizhou Institute of Technology (Grant No.2023GCC021), Guizhou Provincial Science and Technology Projects (Grant No. QiankeheJiChu ZK [2022] yiban 171) and key laboratory of energy chemistry in Guizhou universities (Qian Jiao Ji [2022] 035).

Data Availability Statement: The original contributions presented in the study are included in the article/Supplementary Materials, further inquiries can be directed to the corresponding author/s.

Conflicts of Interest: The authors declare no conflicts of interest.

References

1. Kim, M.G.; Cho, J. Reversible and High-Capacity Nanostructured Electrode Materials for Li-Ion Batteries. *Adv. Funct. Mater.* **2009**, *19*, 1497–1514. [CrossRef]
2. Nitta, N.; Wu, F.X.; Lee, J.T.; Yushin, G.; Lee, G. Yushin, Li-ion battery materials: Present and future. *Mater. Today* **2015**, *18*, 252–264. [CrossRef]
3. Tarascon, J.M.; Armand, M. Issues and challenges facing rechargeable lithium batteries. *Nature* **2001**, *414*, 359–367. [CrossRef]
4. Yoo, H.D.; Markevich, E.; Salitra, G.; Sharon, D.; Aurbach, D. On the challenge of developing advanced technologies for electrochemical energy storage and conversion. *Mater. Today* **2014**, *17*, 110–121. [CrossRef]
5. Armand, M.; Tarascon, J.M. Building better batteries. *Nature* **2008**, *451*, 652–657. [CrossRef]
6. Fang, J.; Yuan, Y.F.; Wang, L.K.; Ni, H.L.; Zhu, H.L.; Gui, J.S.; Yang, J.L.; Chen, Y.B.; Guo, S.Y. Hierarchical ZnO@NiO core–shell nanorod array as high performance anode material for lithium-ion batteries. *Mater. Lett.* **2013**, *111*, 1–4. [CrossRef]
7. Cao, T.; Fang, D.; Liu, L.; Luo, Z.; Wang, Q.; Dong, L.; Xiong, C. Nanosheets-based ZnO–NiO microspheres for lithium-ion batteries. *J. Mater. Sci. Mater. Electron.* **2015**, *26*, 5279–5286. [CrossRef]
8. Xiong, Q.Q.; Tu, J.P.; Xia, X.H.; Zhao, X.Y.; Gu, C.D.; Wang, X.L. A three-dimensional hierarchical Fe_2O_3@NiO core/shell nanorod array on carbon cloth: A new class of anode for high-performance lithium-ion batteries. *Nanoscale* **2013**, *5*, 7906–7912. [CrossRef]
9. Chen, Y.; Cai, R.; Yang, Y.; Liu, C.; Yuan, A.; Yang, H.; Shen, X. Cyanometallic frameworks derived hierarchical porous Fe_2O_3/NiO microflowers with excellent lithium-storage property. *J. Alloys Compd.* **2017**, *698*, 469–475. [CrossRef]
10. Zhang, Y.; Zhuo, Q.; Lv, X.; Ma, Y.; Zhong, J.; Sun, X. NiO-Co_3O_4 nanoplate composite as efficient anode in Li-ion battery. *Electrochim. Acta* **2015**, *178*, 590–596. [CrossRef]
11. Zhong, Y.; Huang, H.; Wang, K.; He, Z.; Zhu, S.; Chang, L.; Shao, H.; Wang, J.; Cao, C.-N. NiO@MnO_2 core–shell composite microtube arrays for high-performance lithium ion batteries. *RSC Adv.* **2017**, *7*, 4840–4847. [CrossRef]
12. Chen, H.; Hu, Z.-L.; Li, C.-L.; Li, N.; Xiang, K.-X. Facile synthesis of CuO–NiO nanocomposites with high surface areas and their application for lithium-ion batteries. *Micro Nano Lett.* **2013**, *8*, 544–548. [CrossRef]
13. Gu, X.; Chen, L.; Ju, Z.; Xu, H.; Yang, J.; Qian, Y. Controlled Growth of Porous α-Fe_2O_3 Branches on β-MnO_2 Nanorods for Excellent Performance in Lithium-Ion Batteries. *Adv. Funct. Mater.* **2013**, *23*, 4049–4056. [CrossRef]
14. Ren, W.; Liu, D.; Sun, C.; Yao, X.; Tan, J.; Wang, C.; Zhao, K.; Wang, X.; Li, Q.; Mai, L. Nonhierarchical Heterostructured Fe_2O_3/Mn_2O_3 Porous Hollow Spheres for Enhanced Lithium Storage. *Small* **2018**, *14*, e1800659. [CrossRef]
15. Novoselov, K.S.; Geim, A.K.; Morozov, S.V.; Jiang, D.; Zhang, Y.; Dubonos, S.V.; Grigorieva, I.V.; Firsov, A.A. Electric field effect in atomically thin carbon films. *Science* **2004**, *306*, 666–669. [CrossRef]
16. Lee, C.; Wei, X.D.; Kysar, J.W.; Hone, J. Measurement of the elastic properties and intrinsic strength of monolayer graphene. *Science* **2008**, *321*, 385–388. [CrossRef] [PubMed]
17. Molitor, F.; Guttinger, J.; Stampfer, C.; Droscher, S.; Jacobsen, A.; Ihn, T.; Ensslin, K. Electronic properties of graphene nanostructures. *J. Phys-Condens. Matter* **2011**, *23*, 212–215. [CrossRef]
18. Wang, Z.; Mu, J.C.; Li, Y.; Chen, J.; Zhang, L.P.; Li, D.G.; Zhao, P.P. Preparation and lithium storage properties of NiO-SnO_2/graphene nanosheet ternary composites. *J. Alloys Compd.* **2017**, *695*, 2909–2915. [CrossRef]
19. Du, D.J.; Yue, W.B.; Fan, X.L.; Tang, K.; Yang, X.J. Ultrathin NiO/$NiFe_2O_4$ Nanoplates Decorated Graphene Nanosheets with Enhanced Lithium Storage Properties. *Electrochim. Acta* **2016**, *194*, 17–25. [CrossRef]
20. Ma, L.; Pei, X.-Y.; Mo, D.-C.; Lyu, S.-S.; Fu, Y.-X. Fabrication of NiO-ZnO/RGO composite as an anode material for lithium-ion batteries. *Ceram. Int.* **2018**, *44*, 22664–22670. [CrossRef]
21. Abbas, S.M.; Hussain, S.T.; Ali, S.; Ahmad, N.; Ali, N.; Abbas, S.; Ali, Z. Modification of carbon nanotubes by CuO-doped NiO nanocomposite for use as an anode material for lithium-ion batteries. *J. Solid. State Chem.* **2013**, *202*, 43–50. [CrossRef]
22. Hummer, W.S.; Offeman, R.E. Preparation of Graphitic Oxide. *J. Am. Chem. Soc.* **1958**, *80*, 1339. [CrossRef]
23. Marcano, D.C.; Kosynkin, D.V.; Berlin, J.M.; Sinitskii, A.; Sun, Z.; Slesarev, A.; Alemany, L.B.; Lu, W.; Tour, J.M. Improved Synthesis of Graphene Oxide. *Acs Nano* **2010**, *4*, 4806–4814. [CrossRef]
24. Song, X.; Sun, S.; Zhang, W.; Yu, H.; Fan, W. Synthesis of $Cu(OH)_2$ Nanowires at Aqueous-Organic Interfaces. *J. Phys. Chem. B* **2004**, *108*, 5200–5205. [CrossRef]
25. Yan, J.; Fan, Z.; Sun, W.; Ning, G.; Wei, T.; Zhang, Q.; Zhang, R.; Zhi, L.; Wei, F. Advanced Asymmetric Supercapacitors Based on $Ni(OH)_2$/Graphene and Porous Graphene Electrodes with High Energy Density. *Adv. Funct. Mater.* **2012**, *22*, 2632–2641. [CrossRef]
26. Yang, W.F.; Cheng, G.H.; Dong, C.Q.; Bai, Q.G.; Chen, X.T.; Peng, Z.Q.; Zhang, Z.H. NiO nanorod array anchored Ni foam as a binder-free anode for high-rate lithium ion batteries. *J. Mater. Chem. A* **2014**, *2*, 20022–20029. [CrossRef]
27. Yang, J.R.; Zeng, D.Q.; Zheng, H.F.; Xie, Q.S.; Huang, J.; Xiao, L.; Peng, D.L. 3D graphene encapsulated ZnO-NiO-CuO double-shelled hollow microspheres with enhanced lithium storage properties. *J. Alloys Compd.* **2018**, *765*, 1158–1166. [CrossRef]
28. Sun, L.; Deng, Q.; Li, Y.; Deng, L.; Wang, Y.; Ren, X.; Zhang, P. Solvothermal synthesis of ternary Cu_2O-CuO-RGO composites as anode materials for high performance lithium-ion batteries. *Electrochim. Acta* **2016**, *222*, 1650–1659. [CrossRef]
29. Hu, L.; Huang, Y.; Zhang, F.; Chen, Q. CuO/Cu_2O composite hollow polyhedrons fabricated from metal-organic framework templates for lithium-ion battery anodes with a long cycling life. *Nanoscale* **2013**, *5*, 4186–4190. [CrossRef]
30. Guo, W.; Sun, W.; Wang, Y. Multilayer CuO@NiO Hollow Spheres: Microwave-Assisted Metal Organic-Framework Derivation and Highly Reversible Structure-Matched Stepwise Lithium Storage. *ACS Nano* **2015**, *9*, 11462–11471. [CrossRef]

31. Yin, H.; Yu, X.-X.; Li, Q.-W.; Cao, M.-L.; Zhang, W.; Zhao, H.; Zhu, M.-Q. Hollow porous CuO/C composite microcubes derived from metal-organic framework templates for highly reversible lithium-ion batteries. *J. Alloys Compd.* **2017**, *706*, 97–102. [CrossRef]
32. Fan, Z.; Liang, J.; Yu, W.; Ding, S.; Cheng, S.; Yang, G.; Wang, Y.; Xi, Y.; Xi, K.; Kumar, R.V. Ultrathin NiO nanosheets anchored on a highly ordered nanostructured carbon as an enhanced anode material for lithium ion batteries. *Nano Energy* **2015**, *16*, 152–162. [CrossRef]
33. Tan, Y.; Li, Q.; Lu, Z.; Yang, C.; Qian, W.; Yu, F. Porous nanocomposites by cotton-derived carbon/NiO with high performance for lithium-ion storage. *J. Alloys Compd.* **2021**, *874*, 159788. [CrossRef]
34. Deng, W.; Chen, X.; Hub, A.; Zhang, S. Graphitic carbon-wrapped NiO embedded three dimensional nitrogen doped aligned carbon nanotube arrays with long cycle life for lithium ion batteries. *Rsc Adv.* **2018**, *8*, 28440–28446. [CrossRef] [PubMed]
35. Wang, C.; Zhao, Y.; Su, D.; Ding, C.; Wang, L.; Yan, D.; Li, J.; Jin, H. Synthesis of NiO Nano Octahedron Aggregates as High-Performance Anode Materials for Lithium Ion Batteries. *Electrochim. Acta* **2017**, *231*, 272–278. [CrossRef]
36. Cui, X.; Song, B.; Cheng, S.; Xie, Y.; Shao, Y.; Sun, Y. Synthesis of carbon nanotube (CNT)-entangled CuO nanotube networks via CNT-catalytic growth and in situ thermal oxidation as additive-free anodes for lithium ion batteries. *Nanotechnology* **2018**, *29*, 035603. [CrossRef] [PubMed]
37. Li, X.; Fan, L.; Li, X.; Shan, H.; Chen, C.; Yan, B.; Xiong, D.; Li, D. Enhanced anode performance of flower-like NiO/RGO nanocomposites for lithium-ion batteries. *Mater. Chem. Phys.* **2018**, *217*, 547–552. [CrossRef]
38. Yin, X.; Chen, H.; Zhi, C.; Sun, W.; Lv, L.P.; Wang, Y. Functionalized Graphene Quantum Dot Modification of Yolk-Shell NiO Microspheres for Superior Lithium Storage. *Small* **2018**, *14*, e1800589. [CrossRef] [PubMed]
39. Chen, J.-X.; Zhao, D.-L.; Yao, R.-R.; Li, C.; Wang, X.-J.; Sun, F.-F. Hedgehog-like CuO/nitrogen-doped graphene nanocomposite for high-performance lithium-ion battery anodes. *J. Alloys Compd.* **2017**, *714*, 419–424. [CrossRef]
40. Wang, Q.; Zhao, J.; Shan, W.; Xia, X.; Xing, L.; Xue, X. CuO nanorods/graphene nanocomposites for high-performance lithium-ion battery anodes. *J. Alloys Compd.* **2014**, *590*, 424–427. [CrossRef]
41. Shi, W.; Zhang, Y.; Key, J.; Shen, P.K. Three-dimensional graphene sheets with NiO nanobelt outgrowths for enhanced capacity and long term high rate cycling Li-ion battery anode material. *J. Power Sources* **2018**, *379*, 362–370. [CrossRef]
42. Park, J.C.; Kim, J.; Kwon, H.; Song, H. Gram-Scale Synthesis of Cu_2O Nanocubes and Subsequent Oxidation to CuO Hollow Nanostructures for Lithium-Ion Battery Anode Materials. *Adv. Mater.* **2009**, *21*, 803–807. [CrossRef]
43. Yuan, W.; Yan, Z.; Pan, B.; Qiu, Z.; Luo, J.; Tan, Z.; Tang, Y.; Li, Z. Hierarchical MCMB/CuO/Cu anode with super-hydrophilic substrate and blind-hole structures for lithium-ion batteries. *J. Alloys Compd.* **2017**, *719*, 353–364. [CrossRef]
44. Ranjbar-Azad, M.; Behpour, M. Facile in situ co-precipitation synthesis of CuO–NiO/rGO nanocomposite for lithium-ion battery anodes. *J. Mater. Sci. Mater. Electron.* **2021**, *32*, 18043–18056. [CrossRef]
45. Liang, J.; Jiang, J.; Xu, M.; Huo, X.; Ye, D.; Zhang, S.; Wu, X.; Wu, W. Improved lithium storage performance of urchin-like CuO microspheres by stereotaxically constructed graphene mediating synergistic effect. *J. Mater. Sci. Mater. Electron.* **2021**, *32*, 8557–8569. [CrossRef]
46. Fu, J.; He, H.; Zeng, T.; Zhang, C. Tunable surface pseudocapacitance assisted fast and flexible lithium storage of graphene wrapped NiO nano-arrays on nitrogen-doped carbon foams. *Electrochim. Acta* **2022**, *407*, 139875. [CrossRef]
47. Bajorowicz, B.; Wilamowska-Zawłocka, M.; Lisowski, W.; Żak, A.; Klimczuk, T. N-doped graphene quantum dot-decorated MOF-derived yolk-shell ZnO/NiO hybrids to boost lithium and sodium ion battery performance. *Appl. Surf. Sci.* **2024**, *655*, 159702. [CrossRef]
48. Ma, L.; Pei, X.Y.; Mo, D.C.; Heng, Y.; Lyu, S.S.; Fu, Y.X. Facile fabrication of NiO flakes and reduced graphene oxide (NiO/RGO) composite as anode material for lithium-ion batteries. *J. Mater. Sci.-Mater.* **2019**, *30*, 5874–5880. [CrossRef]